Sustainable Energy & Fuels

ROYAL SOCIETY OF CHEMISTRY

PAPER

View Article Online
View Journal | View Issue

Open Access Article. Published on 28 March 2023. Downloaded on 12/5/2025 1:32:46 PM.
This article is licensed under a Creative Commons Attribution-NonCommercial 3.0 Unported Licence.

Check for updates

Cite this: *Sustainable Energy Fuels*, 2023, 7, 2270

Correlating nickel functionalities to selectivity for hydrogen peroxide electrosynthesis†

Miha Nosan,[a] Dušan Strmčnik,[b] Vasiliy Brusko,[c] Maria Kirsanova,[d] Matjaž Finšgar,[e] Ayrat M. Dimiev[c] and Boštjan Genorio *[a]

Received 3rd February 2023
Accepted 27th March 2023

DOI: 10.1039/d3se00139c

rsc.li/sustainable-energy

The development of an environmentally friendly, safe and efficient method to produce hydrogen peroxide (H_2O_2) by electrocatalysis is an attractive alternative to the current anthraquinone autoxidation process. In this study, we investigated the morphology, chemical structure, and electrochemical performance of nickel decorated reduced graphene oxide prepared at various heat treatment temperatures in a slightly oxidizing atmosphere. The as-prepared material exhibited atomically dispersed nickel on the surface of reduced graphene oxide (rGO), while materials treated at 300 °C and 900 °C resulted in the formation of larger Ni nanoparticles on rGO. In addition to the morphology and particle size ratios, XRD, ToF SIMS and XPS also revealed the change in nickel/oxygen (Ni–O) functionalities, which led to a different electrochemical performance in terms of ORR activity, stability, and selectivity towards H_2O_2 production. Moreover, a clear correlation between Ni functionalities and selectivity for H_2O_2 production was demonstrated. From the results of this study, new selective electrocatalysts for green electrochemical H_2O_2 production can be designed in the future.

Introduction

Hydrogen peroxide (H_2O_2) is one of the 20 most common industrial chemicals, with annual global production of 4.0 million tons in 2019 with an anticipated increase to 6.0 million tons by the end of 2026.[1] Its main applications are paper and pulp bleaching, precursor in chemical reactions, energy storage agent, green oxidant in wastewater treatment, and as a disinfectant.[2–4] Current H_2O_2 production is based on a multi-step catalytic anthraquinone oxidation–reduction reaction. This large-scale process requires the direct use of hydrogen and oxygen gases, expensive Pd-based catalysts, large amounts of organic solvents, and a complex purification process to remove the solvents and metal impurities from the H_2O_2.[5] Another method for H_2O_2 production is a direct H_2O_2 synthesis from H_2 and O_2 gas by heterogeneous catalysis. Compared to the anthraquinone method, this method does not produce organic waste, but the process is considered dangerous due to direct mixing of H_2 and O_2 gas, as there is a high risk of explosion.[3,6,7] Therefore, a safe and environmentally friendly alternative H_2O_2 production method based on electrochemistry in aqueous electrolytes is being investigated.[8] In the electrochemical method, H_2O_2 can be generated *via* a two electron oxygen reduction reaction (ORR), without flammable H_2 and organic solvents. However, if the electrocatalyst is not selective, then the ORR can proceed *via* a four electron pathway, yielding water which is the undesired product in H_2O_2 production. Therefore, the main challenge in H_2O_2 production is the development of highly selective, stable, and active electrocatalysts.[9]

To date, many different electrocatalysts have been investigated for H_2O_2 production, such as noble metal nanoparticles on carbon supports, noble metal alloys, transition metals, single-atom catalysts, and molecular complexes.[3,10] Among them the highest selectivity for H_2O_2 production has been achieved with graphene derivatives decorated with noble metal–Hg alloys (Ag–Hg, Pd–Hg, Pt–Hg, *etc.*), but the cost of noble metals and Hg toxicity remain major drawbacks for further commercialization.[3] On the other hand, several studies identified graphene based derivatives as H_2O_2 selective non-metal electrocatalysts, but they lack sufficient ORR activity, selectivity and stability.[11–13] To enhance the activity and stability, and to avoid the use of noble metals, a graphene derivative decorated with transition metal nanoparticles is the most reasonable option.[14,15] Among the transition metals, Ni proved to be very promising due to its high electrocatalytic activity and stability. This is very important if the catalyst is to be used in the electrosynthesis of hydrogen peroxide, where it must remain

[a]Faculty of Chemistry and Chemical Technology, University of Ljubljana, Večna pot 113, SI-1000 Ljubljana, Slovenia. E-mail: bostjan.genorio@fkkt.uni-lj.si
[b]The National Institute of Chemistry, Hajdrihova ulica 19, SI-1000 Ljubljana, Slovenia
[c]Laboratory of Advanced Carbon Nanomaterials, Kazan Federal University, Kremlyovskaya Street 18, Kazan420008, Russian Federation
[d]Advanced Imaging Core Facility, Skolkovo Institute of Science and Technology, 121205 Moscow, Russian Federation
[e]Faculty of Chemistry and Chemical Engineering, University of Maribor, Smetanova ulica 17, SI-2000 Maribor, Slovenia

† Electronic supplementary information (ESI) available. See DOI: https://doi.org/10.1039/d3se00139c

This journal is © The Royal Society of Chemistry 2023

Open Access Article. Published on 28 March 2023. Downloaded on 12/5/2025 1:32:46 PM.
This article is licensed under a Creative Commons Attribution-NonCommercial 3.0 Unported Licence.

active for extended periods of time.[8] Also very important are the low cost and abundance of nickel in general, which make Ni a cost-effective electrocatalyst, that is attractive for commercialization. Finally, the properties of Ni can be tuned by controlling its synthesis, which allows optimization of its electrocatalytic selectivity. In particular, Ni in the form of single atoms[12,16–19] or amorphous NiO nanosheets,[20] showed high selectivity for the ORR for H_2O_2 production, although a correlation between Ni functional groups and electrochemical performance has not yet been established.

In this work, we compare the ORR efficiency towards H_2O_2 production between different nickel-functionalities on reduced graphene oxide electrocatalysts (Ni@rGO). The Ni@rGO electrocatalysts were synthesized using the same starting materials but different heat treatment protocols in a slightly oxidative atmosphere. All synthesized materials were characterized morphologically, chemically, and electrochemically to investigate the influence of nickel/oxygen (Ni–O) functionalities on selectivity. In addition, we directly correlated concentration of Ni–O functionalities with ORR selectivity in alkaline electrolytes. The results of the present study pave the way towards the development of an efficient and cost-effective electrocatalyst for H_2O_2 production.

Experimental section

Materials

KOH (Fluka, TraceSELECT, ≥99.995 wt%), 2-propanol (MiliporeSigma, HPLC grade, ≥99.7 wt%), and Nafion (Merck, 5 wt%) perfluorinated resin solution were used as received. All dissolutions and dispersions were performed with ultrapure water obtained from a Milli-Q system (Millipore) with a resistivity of 18.2 MΩ cm. Sulfuric acid (96 wt%, Shchekinoazot LLC, Russia), hydrochloric acid (35 wt%, TatKhimProduct CJSC, Russia), potassium permanganate (99.5 wt%, MCD Company, Russia), sodium tetrahydroborate $NaBH_4$, nickel nitrate $Ni(NO_3)_2$ (99.5 wt%, TatKhimProduct CJSC), and graphite flakes (90 wt%, TatKhimProduct CJSC) were used without further purification.

Synthesis of GO

Graphite flakes (4 g, 0.33 mol) were dispersed in 92 wt% sulfuric acid (240 mL) at room temperature using a mechanical stirrer. The use of the 92 wt% acid increases the rate of the reaction approx. 8 times compared to the 98 wt% acid.[21] After 10 min of stirring, $KMnO_4$ (4 g, 25.3 mmol) was added to the mixture. The mixture became green due to the conversion of $KMnO_4$ to the permanganyl cation (MnO^{3+}). Additional portions of $KMnO_4$ (4 g, 25.3 mmol each) were added sequentially when the green color of MnO^{3+} was diminished indicating that the previous portion of the oxidizing agent was consumed. In total, 3.6 wt equivalents of $KMnO_4$ were sequentially added. After full consumption of $KMnO_4$, the reaction was quenched with 700 mL of ice–water mixture and stirred for 1 h. Next, 30 wt% H_2O_2 solution was added dropwise (approx. 4 mL) to convert insoluble manganese by-products to soluble colorless Mn(II) ions. This converts the color of the reaction mixture from pinkish to bright yellow. The reaction mixture was centrifuged for 20 min at 5000 rpm to separate GO from the diluted acid. For purification, the GO precipitate was redispersed in distilled water, stirred for 60 min, and centrifuged for 40 min at 5000 rpm to precipitate purified GO from washing waters. This procedure constitutes one purification cycle. Four more purification cycles were performed consecutively. 4 wt% solution of HCl was added at the end of the last three purification cycles. The GO precipitate after the last washing was dried in air. As a result, 7.6 g of air-dried GO was obtained.

Preparation of Ni@rGO

Impregnation step. To prepare the GO/Ni^{2+} composite, 1.0 g GO dispersed in 50 mL water was mixed with the $Ni(NO_3)_2$ solution, containing 0.75 g of Ni^{2+} ions. The dispersion was stirred for 2 h and then centrifuged to separate the as-formed GO/Ni^{2+} intermediate product from the excess of non-reacted $Ni(NO_3)_2$.

Chemical reduction. The pasty GO/Ni^{2+} precipitate, obtained after the centrifugation, was redispersed in 500 mL distilled water. The solution was transferred to a round-bottom flask, equipped with a condenser. Then, sodium tetrahydroborate ($NaBH_4$) 4.0 g was added in portions for 15 min, and the solution was stirred at 90 °C for 3 h until the release of the gas stopped. During this step, GO was visibly blackened and coagulated. After the reaction, the mixture was filtered through a PTFE membrane filter and washed on the filter with water. The purified product was dried under ambient conditions. The yield was 0.70 g. The as-prepared product was denoted as Ni@rGO.

Preparation of Ni@rGO 300 and Ni@rGO 900

The as-obtained Ni@rGO was annealed in a tubular furnace in a slightly oxidative flow of nitrogen. The nitrogen purity was 99.99%, so in addition to nitrogen, the gaseous mixture contained 0.01 vol% of oxygen. The two samples annealed for 20 min at 300 °C and 900 °C were denoted as Ni@rGO 300 and Ni@rGO 900, respectively.

Preparation of the thin film working electrode (WE)

The catalyst ink was prepared by mixing the electrocatalytically active material (Ni@rGO, Ni@rGO 300 or Ni@rGO 900), ultrapure water, 2-propanol (IPA), and Nafion (5 wt% water resin) in a ratio of 4.5 mg : 0.8 mL : 0.3 mL : 30.0 μL, respectively. The mixture was then homogeneously dispersed with a horn sonicator (37.5 W). Finally, an aliquot of 25 μL of the mixture was applied to a glassy carbon disk electrode (diameter = 5.5 mm) on an inverse rotating ring disk electrode (RRDE), equipped with a gold ring electrode at a speed of 300 rpm at room temperature for 45 min. The electrode thus prepared was then used in all electrochemical experiments.

Scanning electron microscopy (SEM)

Images were acquired with a Merlin field-emission high-resolution scanning electron microscope from Carl Zeiss at an

Open Access Article. Published on 28 March 2023. Downloaded on 12/5/2025 1:32:46 PM.
This article is licensed under a Creative Commons Attribution-NonCommercial 3.0 Unported Licence.

accelerating voltage of incident electrons of 5 kV and a current probe of 300 pA.

Transmission electron microscopy (TEM)

Bright field TEM (BF-TEM) and high angle annular dark field scanning transmission electron microscopy (HAADF-STEM) images were acquired with a Titan Themis Z microscope equipped with a DCOR+ spherical aberration corrector and operated at 200 kV. BF-TEM images were recorded using a BM-Ceta 4 K × 4 K CMOS camera with 2 pixel binning. The noise in the BF-TEM images was suppressed either by applying a low-pass Fourier filter or by averaging a few experimental images taken with short dwell time. Energy-dispersive X-ray (EDX) spectra and elemental maps were collected in the STEM mode using a Super-X system, consisting of four large-area ring-shaped SSD detectors. The EDX spectra and maps were processed with the Velox software.

X-Ray photoelectron spectroscopy (XPS) measurements

XPS measurements were performed using a Supra plus spectrometer (Kratos, Manchester, UK) equipped with a hemispherical analyzer and a monochromatic Al K_α X-ray source. Survey spectra were measured at a pass energy of 160 eV with a step of 1 eV. High-resolution spectra were measured at a pass energy of 20 eV at a step of 0.1 eV. The data were acquired using the ESCApe 1.4 software. Fitting of the high-resolution XPS spectra was performed using CasaXPS software with Shirley background subtraction using 30–70% Gaussian–Lorentzian peak shapes. The binding energy was corrected using the C–C/C–H peak in the C 1s spectra at 284.5 eV. The fitting of Ni $2p^{3/2}$ spectra was performed using the parameters in Table S1,† where peak energy and FWHM constraints were taken as ±0.2 eV around the values reported previously.[22–26] The O 1s and C 1s high-resolution spectra fitting was performed similarly.[25,27]

X-Ray diffraction (XRD)

Performed with a Bruker D8 Advance with Cu Kα irradiation (λ = 1.5418 Å) in the Bragg–Brentano geometry; the rate was 0.18° min^{-1}; the range of 2θ angle was from 7° to 100°; the step was 0.015°.

Time-of-flight secondary ion mass spectrometry (ToF-SIMS)

An M6 instrument (IONTOF, Münster, Germany) was employed for ToF-SIMS measurements. During the spectra acquisition, the charge neutralizer (flood gun) was on, a surface potential was applied, and the Ar flooding at 5×10^{-7} mbar in the main analysis chamber was carried out. Analyses were performed using the 30 keV Bi^+ primary ion beam at the target current of 1.1 pA on a 100 by 100 μm spot size. Measurements and data processing were performed with SurfaceLab 7.3 (IONTOF). The mass spectra were corrected using known signals in the positive and negative polarity. To correct the spectra in the positive polarity, the signals for CH_3^+ at m/z 15.02, $C_2H_5^+$ at m/z 29.04, $C_4H_5^+$ at m/z 53.04, $C_4H_9^+$ at m/z 57.07, and $C_5H_9^+$ at m/z 69.07 were used, whereas, in the negative polarity, the signals for C^- at m/z 12.00, C_2^- at m/z 24.00, C_3^- at m/z 36.00, and C_4^- at m/z 48.00 were employed.

Electrochemical characterization

ORR activity. Cyclic voltammetry (CV) measurements were performed with a PGSTAT30 (Autolab) potentiostat/galvanostat with a three-electrode system using a Ag/AgCl (3 M NaCl) reference electrode (RE) supplied by Basi Research Products RE 5B, mixed metal oxide (IrO_2 and TiO_2 on a Ti support, Specialist Casting) as the counter electrode, and a rotating ring disk electrode (RRDE) (Pine Research) with a glassy carbon disk and gold ring electrode as the working electrode. RRDE experiments were performed at 1600 rpm on a WaveVortex 10 (Pine Research) rotation control unit. For all electrochemical experiments, an aqueous 0.1 M KOH electrolyte was saturated with either Ar (purity 5.0) or O_2 (purity 4.6) and a scan rate of 20 mV s^{-1} was used. The electrolyte resistance was determined by the positive feedback method before each measurement and compensation of the total solution resistance (90%) was performed. All potentials in this work are referred to the RHE (V *vs.* RHE). Before each measurement, the potential of the Ag/AgCl (3 M NaCl) RE was checked by measuring the open circuit potential of the reference electrode with respect to a platinum wire, both immersed in an H_2-saturated 0.1 M KOH solution. In addition, the gold ring electrode was electrochemically cleaned for 15 min at an applied potential of −0.20 V *vs.* RHE before RRDE measurement. This was done to remove any oxides formed on the ring electrode prior to selectivity measurement. The ORR activity of the materials was compared using the kinetic current density (J_K) in mix current density region at E = 0.6 V *vs.* RHE.

ORR selectivity. The ORR selectivity was determined with the RRDE. The potential at the disk electrode was swept in the cathodic direction (1.1–0.1 V *vs.* RHE), while the potential of the ring electrode was held at E = 1.3 V *vs.* RHE. The number of transferred electrons per reduced oxygen molecule (n) was calculated using the $n = 4 \times i_d/(i_d - i_r/N_c)$ equation.

where i_d is the disk current, i_r is the ring current, and N_c (0.38) is the collection efficiency. N_c was determined in 10 mM $Fe(CN)_6^{3-}/Fe(CN)_6^{4-}$ at 1600 rpm in 0.1 M KOH solution. Further, the H_2O_2 faradaic efficiency (%) was determined using the $\%H_2O_2 = 100 \times (4 - n)/2$ equation.

Electrochemical stability. The chronoamperometric (CA) stability measurements were performed at potential 0.50 V *vs.* RHE with the RDE in O_2 saturated 0.1 M KOH at 1600 rpm for 2 hour.

Results and discussion

Synthesis and characterization (morphological, chemical and spectroscopic)

To synthesize Ni@rGO electrocatalysts with different nickel/oxygen (Ni–O) functionalities on a graphene-based support, we used different heat treatment protocols in a slightly oxidizing N_2 atmosphere. In the following steps all three materials (Ni@rGO, Ni@rGO 300 and Ni@rGO 900) were

Open Access Article. Published on 28 March 2023. Downloaded on 12/5/2025 1:32:46 PM.
This article is licensed under a Creative Commons Attribution-NonCommercial 3.0 Unported Licence.

subjected to thorough morphological, structural, chemical, and electrochemical characterization. To understand the morphological and chemical characteristics of the prepared materials, we performed SEM, TEM, and EDXS analyses. The SEM images of Ni@rGO and Ni@rGO 900 are shown in Fig. 1a and b, respectively. It can be clearly seen that both materials have similar wrinkled morphology that is typical for reduced graphene oxide (rGO). However, in Fig. 1b brighter spots can be seen on Ni@rGO 900 which represent Ni nanoparticles (NPs) formed on the rGO surface during the heat-treatment process. This was further supported by TEM (Fig. 1c and d), where a clear difference between Ni@rGO, and Ni@rGO 900 can be seen. Fig. 1c shows that Ni@rGO does not contain any distinguishable particles even at the highest magnification. At the same time, the EDXS mapping (Fig. 1e) shows that Ni is homogenously distributed over the sample on the atomic level. Similar observations have been made in previous studies.[28,29] Finally, EDXS mapping for Ni@rGO 900 shows relatively large irregular-shaped Ni NPs with a diameter of approximately 50 nm to 100 nm (Fig. 1f). Compared to Ni@rGO 900, Ni@rGO 300 shows a similar irregular NP shape but smaller dimensions between 20 and 30 nm (Fig. S1a†). According to the TEM images, we can conclude that Ni surface diffusion enabled Ni nucleation, aggregation, and crystallization which were more pronounced at higher temperatures. More TEM images with different magnifications for Ni@rGO, Ni@rGO 300 and Ni@rGO 900 can be found in the ESI, Fig. S2–S4,† respectively.

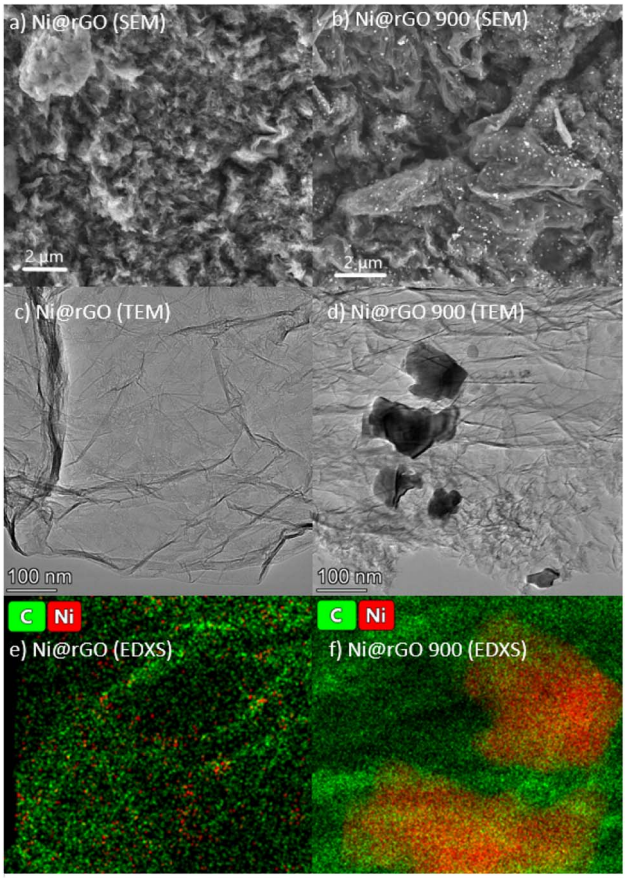

Fig. 1 SEM images of (a) Ni@rGO and (b) Ni@rGO 900, TEM images of (c) Ni@rGO and (d) Ni@rGO 900 and EDXS of (e) Ni@rGO and (f) Ni@rGO 900 materials.

A series of bright-field TEM images of the Ni@rGO 900 material in Fig. S5a–d† illustrate the shape and size of nanoparticles at different magnifications. The electron diffraction (ED) image (Fig. S5e†) obtained from the group of particles shown in Fig. S5a† is a superposition of the ring diffraction of graphene domains (interplanar distances of 2.18 and 1.23 Å) and the point reflections corresponding to interplanar distances of ~2.40 Å, 2.08 Å, 1.47 Å, and 1.25 Å, consistent with the {111}, {200}, { 220} and {311} face-centered cubic NiO cell with parameter $a = 4.12$ Å. The ED image shown in Fig. S5f,† obtained from the individual polygonal particle shown in Fig. S5c† contains only point reflections of the NiO lattice and is a superposition of the diffraction patterns of nanodomains oriented along the [001] and [011] directions.

In order to obtain detailed information about the chemical composition and Ni–O functionalities of the prepared materials, XRD, ToF-SIMS, and XPS measurements were performed. In the XRD diffractograms of Ni@rGO (black curve) and Ni@rGO 300 (red curve) in Fig. 2a four broad peaks at $2\theta = 34.0°$, 43.3°, 60.3°, and 78.5° can be seen, all corresponding to Ni functionalities. In contrast, sharp peaks were detected for Ni@rGO 900 (blue curve) where relatively large NPs were observed with SEM and TEM. Based on the crystal structure database, sharp peaks were assigned to the Ni and NiO crystal planes. The same NiO crystal planes for Ni@rGO 900 were confirmed by ED as shown in Fig. S5f,† with additional Ni {110}, {111}, {200}, {222} and {311}. Another observation that can be extracted from the XRD diffractograms is the shift of the graphite (002) peak from $2\theta = 23.2°$ (Ni@rGO) < $2\theta = 25.3°$ (Ni@rGO 300) < $2\theta = 26.3°$ (Ni@rGO 900), which is characteristic for oxygen removal from the rGO and consequently narrowing the interplanar distances (L_c) between graphene layers towards crystalline graphite (002) at $2\theta = 26.4°$.[30] The latter is also related to the enhanced rGO electrical conductivity and was evaluated previously.[31] Investigation of the surface Ni functionalities was performed by ToF-SIMS analysis in negative polarity (Fig. 2b–d). ToF-SIMS measurements revealed at least three different Ni functional groups for all three samples: Ni, NiO, and $Ni(OH)_2$ at m/z 57.92 (signal for Ni^-), 73.92 (signal for NiO^-), and 91.94 (signal for $Ni(OH)_2^-$), respectively. In addition, it should be noted that ToF SIMS can indirectly provide insight into the interaction of Ni-based NPs with the rGO substrate through Ni–O–C bonding or O–Ni–C bonding. The presence of secondary ions such as $NiCOO^-$ and $NiCO^-$ in the negative polarity and $NiCOO^+$ and $NiCO^+$ in the positive polarity could be related to the electrochemical stability of the electrocatalyst. Fig. S6† shows the presence of all secondary ions for Ni@rGO 300 and Ni@rGO900, but the absence of the $NiCO^-$ peak in negative polarity and $NiCOO^+$ and $NiCO^+$ in positive polarity for Ni@rGO, indicating possible stronger Ni–O–C interaction ($NiCOO^-$) for Ni@rGO 300 and Ni@rGO900 compared with Ni@rGO. It should be noted, however, that ToF-SIMS is not a quantitative technique because the matrix can affect the intensity of the analyte peaks, with a high atomic number matrix absorbing or scattering the primary ion beam and thus reducing

Open Access Article. Published on 28 March 2023. Downloaded on 12/5/2025 1:32:46 PM.
This article is licensed under a Creative Commons Attribution-NonCommercial 3.0 Unported Licence.

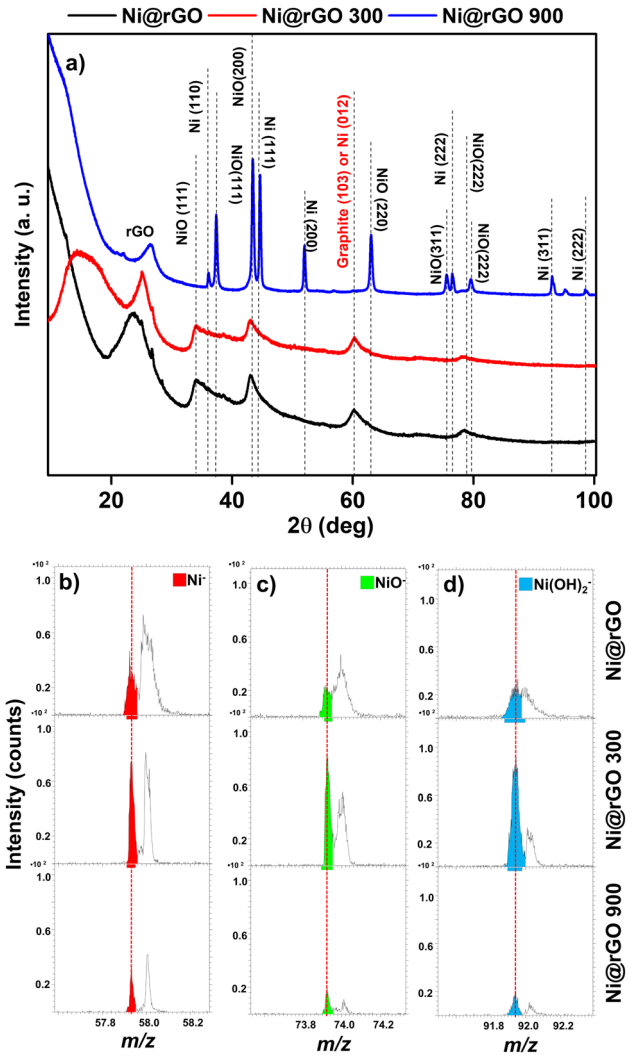

Fig. 2 (a) XRD diffractograms of Ni@rGO (black curve), Ni@rGO 300 (red curve), and Ni@rGO 900 (blue curve) with labelled crystal planes for rGO, Ni, and NiO. The negative ion ToF-SIMS spectra with marked signals for (b) Ni^-, (c) NiO^-, and (d) $Ni(OH)_2^-$ for the Ni@rGO (upper), Ni@rGO 300 (middle), and Ni@rGO 900 (lower) samples.

the number of secondary ions detected.[32] This effect is seen to some extent for Ni@rGO 900 (Fig. 2b–d) with the largest NPs. Based on the XRD and ToF-SIMS results, the XPS $2p^{3/2}$ peak was fitted accordingly to evaluate Ni-functionalities quantitatively.

Similar to ToF SIMS, XPS is also a surface method. In this regard, the surface atomic concentrations were determined from the survey XPS spectra (Fig. S7†) and are summarized in Table 1. Table 1 indicates that the atomic surface concentration of O decreases with higher temperatures of the heat-treatment protocol. This is due to the thermal decomposition of oxygen groups in rGO at higher temperatures. The O at% concentration decreased (Table 1) from 14.56 at% (Ni@rGO), to 8.89 at% (Ni@rGO 300) and 7.95 at% (Ni@rGO 900). Fig. S8 and S9† show high-resolution O 1s and C 1s spectra, respectively, demonstrating that most of the remaining O functionalities are bound to the rGO substrate for all three materials. Moreover, the at% O bound to Ni corresponds to the at% concentration of the relevant Ni species. Oxygen removal affected the increased at% Ni surface concentration for Ni@rGO 300 and Ni@rGO 900, as shown in Fig. 3a. When most of the oxygen is removed, the at% of Ni is generally similar, as shown in Fig. 3a by comparing the at% O and at% Ni. The XPS survey spectra also revealed the presence of fluorine impurities in the Ni@rGO and Ni@rGO 300 materials. The presence of fluorine contamination originates from the PTFE membrane filter, which was used in the work up procedure. The Ni functionalities were investigated by core level Ni $2p^{3/2}$ spectra peak fitting (Fig. 3a–c). Peak fitting of Ni $2p^{3/2}$ was performed based on the evaluation of surface composition using XRD and ToF-SIMS spectra shown in Fig. 2. Fitting of the Ni 2p spectra was performed by employing three peaks for Ni, five for NiO, and six for $Ni(OH)_2$ with predetermined peak area ratios, FWHM, and peak positions, as reported previously.[22–26] The fitting parameters for NiO and $Ni(OH)_2$ peaks in the Ni $2p^{3/2}$ spectra are given in the ESI (Table S3†). The results presented in Fig. 3a–c and summarized in Table 1 show that by increasing the synthesis temperature the amount of $Ni(OH)_2$ decreases while the amount of NiO increases.

Electrochemical characterization

ORR activity and selectivity. The electrochemical characterization of the Ni@rGO, Ni@rGO 300, and Ni@rGO 900 materials was performed. The blank sample CV, which was performed in Ar-saturated solution, is shown in Fig. S10,† and shows the same shape of voltammograms with similar specific capacitance values. First, the performance of the ORR activity was evaluated. This was done using the electrocatalyst in 0.1 M KOH saturated with O_2, which is shown in Fig. 4a. The highest J_K @ 0.6 V *vs.* RHE, and thus the highest activity (Fig. 4c) was obtained for Ni@rGO 900 with 8.17, for Ni@rGO 300 with 3.79, and for Ni@rGO with 2.40 mA cm^{-2}_{GEO}.

Table 1 Atomic surface concentration (at%) of C, O, and Ni normalized to 100.0 at% determined using XPS survey spectra. The at% of NiO, $Ni(OH)_2$ and Ni, was determined by the Ni $2p^{3/2}$ peak fitting and is reported relative to total Ni $2p^{3/2}$ peak area. In the last column, J_K @ 0.6 V *vs.* RHE in 0.1 M KOH for Ni@rGO, Ni@rGO 300, and Ni@rGO 900 is reported

Material	C (at%)	O (at%)	Ni (at%)	NiO (at% Ni)	$Ni(OH)_2$ (at% Ni)	Ni (at% Ni)	J_K @ 0.6 V *vs.* RHE (mA cm^{-2}_{GEO})
Ni@rGO	84.02	14.56	0.78	5.28	94.72	0.00	2.40
Ni@rGO 300	89.31	8.89	1.40	31.33	68.50	0.17	3.70
Ni@rGO 900	90.84	7.95	1.21	97.19	0.00	2.81	8.17

 This journal is © The Royal Society of Chemistry 2023

Open Access Article. Published on 28 March 2023. Downloaded on 12/5/2025 1:32:46 PM.
This article is licensed under a Creative Commons Attribution-NonCommercial 3.0 Unported Licence.

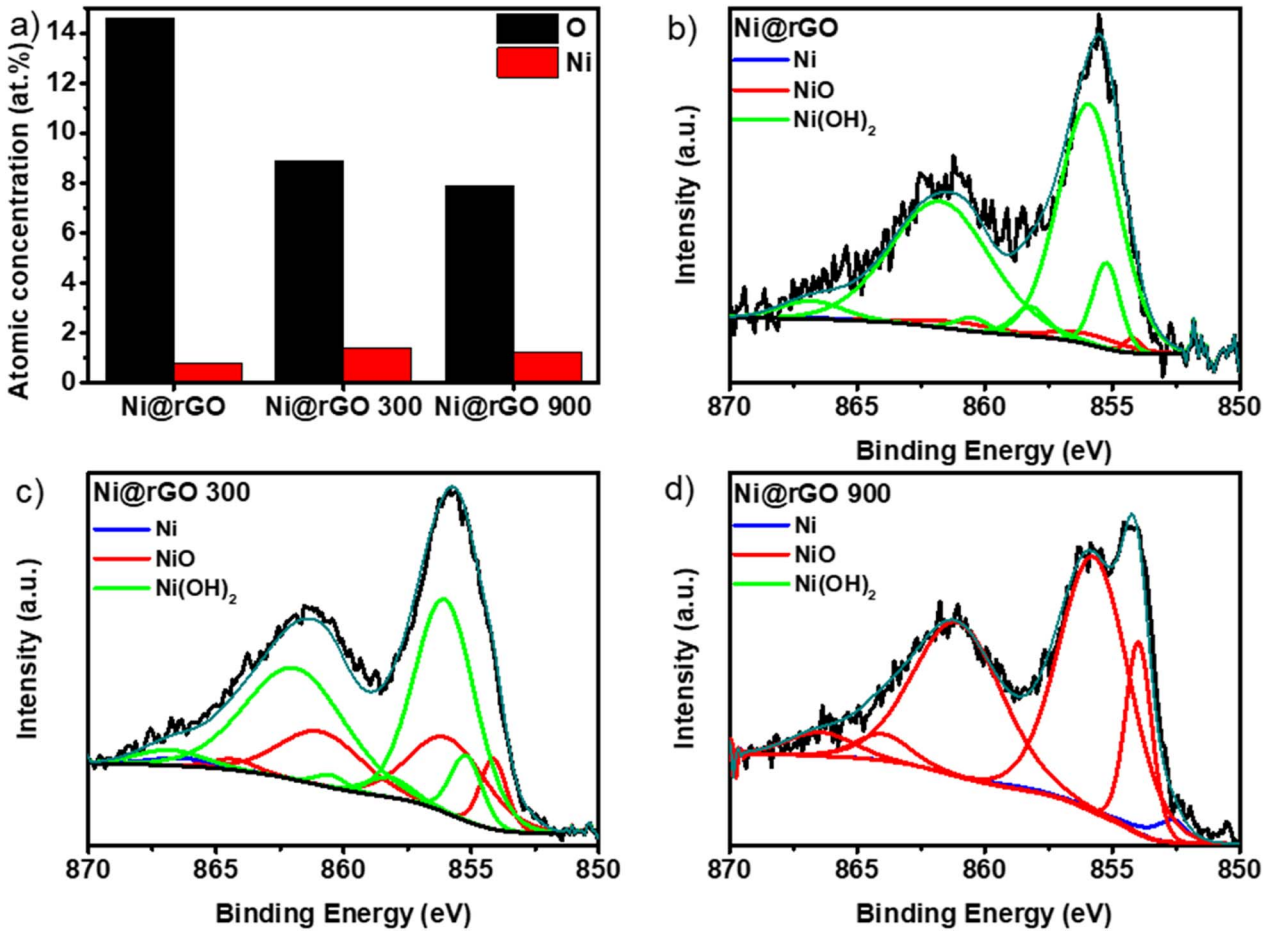

Fig. 3 (a) The atomic surface concentration of O and Ni, and the XPS fitting of the Ni $2p_{3/2}$ spectra for (b) Ni@rGO, (c) Ni@rGO 300, and (d) Ni@rGO 900.

A proportional relationship was found between the synthesis temperature and the activity of the electrocatalyst studied. The higher the final temperature, the higher the activity. The heat treatment protocol affects at least three parameters: (i) conductivity, (ii) NP size, (iii) Ni functionalities. Higher temperatures increase the electrical conductivity of the rGO substrate due to the loss of oxygen functionalities (Table 1) of the rGO and the restoration of the sp^2-graphene structure (Fig. S9†).[31] Higher temperatures increase the particle size (Fig. 1) and change the composition and concentration of Ni functionalities (Fig. 3). However, with the present study, we are not able to determine which of the three parameters is responsible for the increased J_K. We can conclude that the increased conductivity, the increased particle size and the high concentration of NiO species have a positive influence on the increased activity, which is most clearly expressed in the case of Ni@rGO 900.

Next, the ORR selectivity in the 0.1–0.9 V *vs.* RHE potential range was determined by evaluating the concentration of H_2O_2 (%H_2O_2) detected by the RRDE (Fig. 4b). The selectivity was then compared at $E = 0.5$ V *vs.* RHE. The highest %H_2O_2 production efficiency was observed for Ni@rGO 900 with 89% H_2O_2 followed by Ni@rGO 300 with 76% H_2O_2 and Ni@rGO with 62%.

Interestingly, a correlation was identified when %H_2O_2 *vs.* at% of NiO was plotted. Linear correlation fit gave a squared correlation coefficient, R^2, of 0.93 (Fig. 5). This may indicate that the increase of NiO functionalities contributes to increased electrocatalyst selectivity and H_2O_2 production efficiency. This finding is very important and will help to develop highly selective electrocatalysts for H_2O_2 electrosynthesis in the future.

ORR stability. Finally, the stability of the electrocatalyst was tested by chronoamperometry (CA) for 2 hours at a potential of $E = 0.50$ V *vs.* RHE (Fig. 4d). This potential was chosen at the maximum %H_2O_2 production potential. From the stability studies (Fig. 4d), Ni@rGO 300 and Ni@rGO 900 had the best performance with a current loss of 4.5% after 2 hours. This is also in correspondence with ToF SIMS results (Fig. S6†), where secondary ions indicating strong interaction between Ni and rGO were identified. Ni@rGO was on the other hand less stable, with a current loss of 8.9%. This was to be expected, as single atoms are usually less stable than NPs shown previously.[33]

To check how the stability test affects the selectivity of the electrocatalysts, the selectivity measurement was repeated after

Open Access Article. Published on 28 March 2023. Downloaded on 12/5/2025 1:32:46 PM.
This article is licensed under a Creative Commons Attribution-NonCommercial 3.0 Unported Licence.

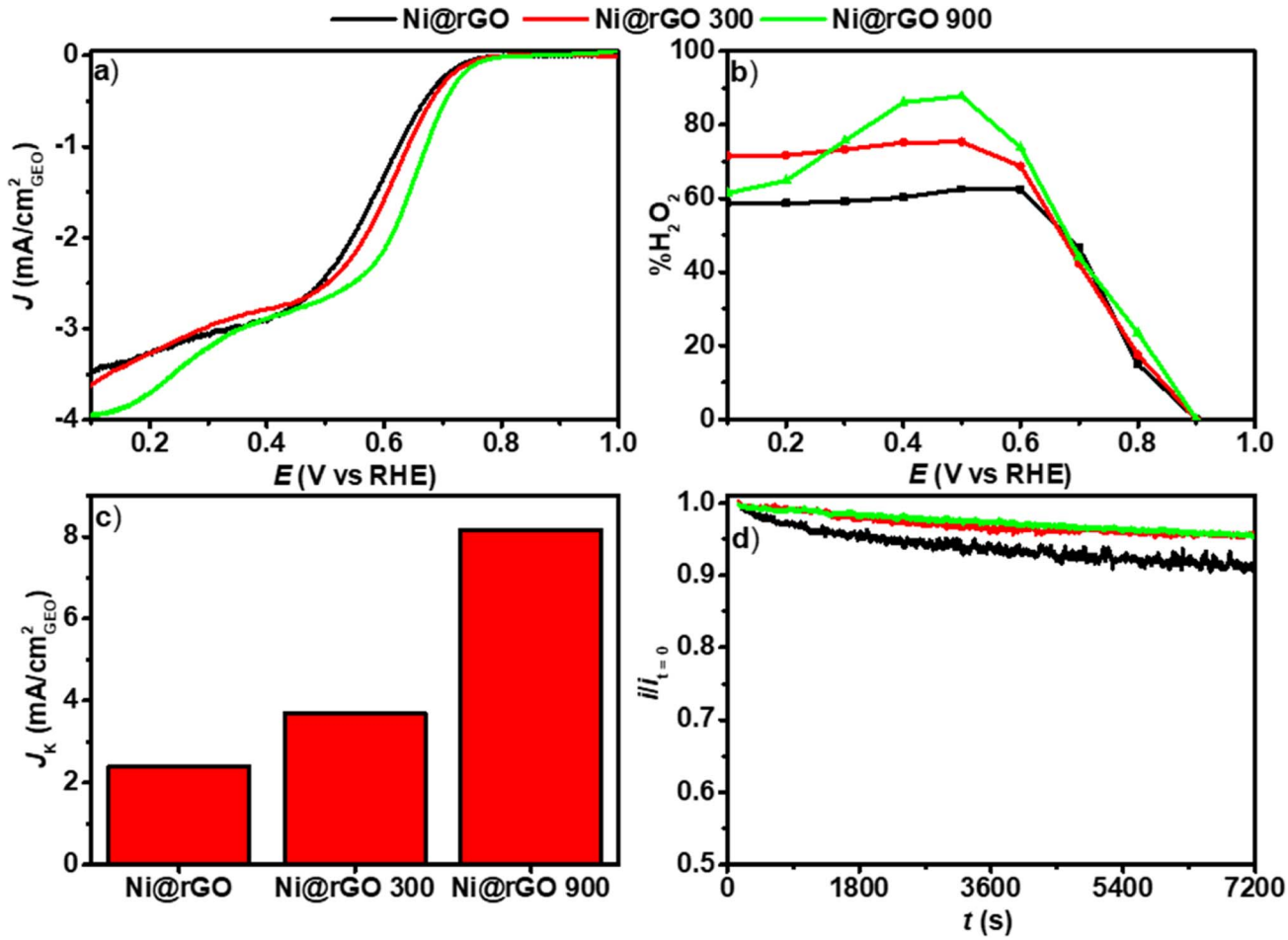

Fig. 4 Electrochemical measurements of Ni@rGO (black curves), Ni@rGO 300 (red curves), and Ni@rGO 900 (green curves); (a) ORR polarization curves (b) %H_2O_2 production efficiency, (c) kinetic current density @ $E = 0.6$ V *vs.* RHE and (d) two-hour chronoamperometry stability measurement at 0.5 V *vs.* RHE. Electrochemical RDE and RRDE measurements were performed in O_2 saturated 0.1 M KOH solution at a potential scan rate of 20 mV s^{-1} and 1600 rpm.

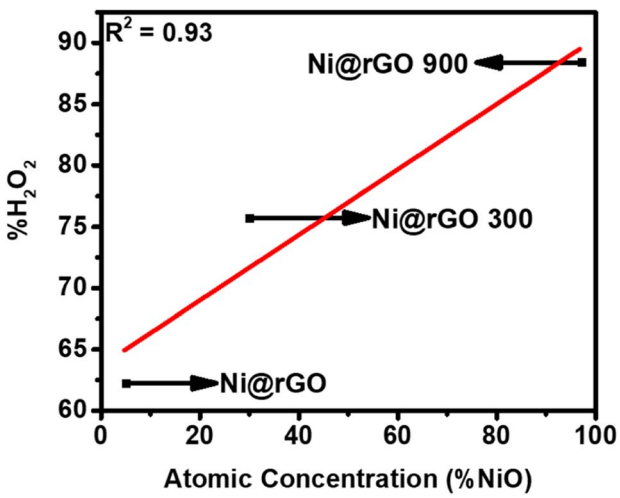

Fig. 5 The linear fitting trend of %H_2O_2 produced relative to NiO at% surface concentration for Ni@rGO, Ni@rGO 300, and Ni@rGO 900 at $E = 0.50$ V *vs.* RHE.

the two-hour CA (Fig. S11b–d†). The results show that there was almost no change in the selectivity of the electrocatalysts. The electrocatalyst performance difference between before and after CA is 2–3% which is within the experimental error.

Conclusion

We synthesized and characterized Ni-decorated rGO electrocatalysts heat-treated at different temperatures in a mildly oxidative atmosphere (0.1 vol% O_2 in N_2). Morphological and chemical analyses revealed different sizes of nanoparticles and types of Ni–O functionalities. The as prepared Ni@rGO samples had a homogeneous morphology with Ni nanoparticles atomically distributed on the rGO surface. With the increasing heating temperature, the O concentration of the sample decreased, and at the same time, the remaining Ni atoms thermally diffused and agglomerated into larger oxidized Ni nanoparticles (NPs). The largest NPs were found at the highest temperature. XRD, ToF-SIMS, and XPS measurements revealed Ni, NiO and $Ni(OH)_2$ as well as other Ni functional species on the rGO substrate. Electrochemical studies showed increased activity

 This journal is © The Royal Society of Chemistry 2023

Open Access Article. Published on 28 March 2023. Downloaded on 12/5/2025 1:32:46 PM.
This article is licensed under a Creative Commons Attribution-NonCommercial 3.0 Unported Licence.

and selectivity for H_2O_2 production for the materials synthesized at higher temperatures, with Ni@rGO 900 showing the best performance in terms of activity, stability, and selectivity. The correlation of the Ni-functionalities and their concentrations with the electrochemical results, especially the selectivity, revealed an interesting trend. The increased H_2O_2 selectivity and production efficiency were linearly correlated with NiO atomic concentration. The presented results are indicative of the future development of more efficient and selective electrocatalysts for H_2O_2 electrosynthesis.

Author contributions

M. N.: investigation, data curation, visualization, writing, original draft preparation, reviewing and editing. B. G.: supervision, visualization, methodology, project administration, funding acquisition, writing, data curation, investigation, reviewing and editing. A. D.: supervision, data curation, reviewing and editing. M. F.: data curation, reviewing and editing. D. S.: reviewing and editing. All authors contributed to the final version of this paper.

Conflicts of interest

There are no conflicts to declare.

Acknowledgements

This work was funded by the Slovenian Research Agency (ARRS) through the Research Funding Programmes P1-0175, P2-0423, P2-0393, and P2-0118, Research project J7-4636, and Bilateral Research Project N2-0087 and BI-RU/19-20-025 – Synthesis and characterization of nanocatalyst electrodes for HER and ORR reactions. The authors also acknowledge the support of the Centre for Research Infrastructure at the University of Ljubljana, Faculty of Chemistry and Chemical Technology, which is part of the Network of Research and Infrastructural Centres UL (MRIC UL) and is financially supported by the Slovenian Research Agency (Infrastructure programme No. I0-0022).

References

1 Y. Jia, Y. Bai, J. Chang, Y. Zhai, T. Zhang, K. Ren and J. Hong, *J. Cleaner Prod.*, 2022, **352**, 131655.
2 M. Batzill, *Surf. Sci. Rep.*, 2012, **67**, 83–115.
3 N. Wang, S. Ma, P. Zuo, J. Duan and B. Hou, *Adv. Sci.*, 2021, **8**, 1–26.
4 R. Ciriminna, L. Albanese, F. Meneguzzo and M. Pagliaro, *ChemSusChem*, 2016, **9**, 3374–3381.
5 K. Jiang, S. Back, A. J. Akey, C. Xia, Y. Hu, W. Liang, D. Schaak, E. Stavitski, J. K. Nørskov, S. Siahrostami and H. Wang, *Nat. Commun.*, 2019, **10**, 3997.
6 P. V. Kumar, N. M. Bardhan, G. Y. Chen, Z. Li, A. M. Belcher and J. C. Grossman, *Carbon*, 2016, **100**, 90–98.
7 C. Samanta, *Appl. Catal., A*, 2008, **350**, 133–149.
8 P. F. B. D. Martins, I. Plazl, D. Strmcnik and B. Genorio, *Curr. Opin. Electrochem.*, 2023, **38**, 101223.
9 H. W. Kim, V. J. Bukas, H. Park, S. Park, K. M. Diederichsen, J. Lim, Y. H. Cho, J. Kim, W. Kim, T. H. Han, J. Voss, A. C. Luntz and B. D. McCloskey, *ACS Catal.*, 2020, **10**, 852–863.
10 S. Yang, A. Verdaguer-Casadevall, L. Arnarson, L. Silvioli, V. Čolić, R. Frydendal, J. Rossmeisl, I. Chorkendorff and I. E. L. Stephens, *ACS Catal.*, 2018, **8**, 4064–4081.
11 G. Passard, D. K. Dogutan, M. Qiu, C. Costentin and D. G. Nocera, *ACS Catal.*, 2018, **8**, 8671–8679.
12 Y. Sun, L. Silvioli, N. R. Sahraie, W. Ju, J. Li, A. Zitolo, S. Li, A. Bagger, L. Arnarson, X. Wang, T. Moeller, D. Bernsmeier, J. Rossmeisl, F. Jaouen and P. Strasser, *J. Am. Chem. Soc.*, 2019, **141**, 12372–12381.
13 K. H. Wu, D. Wang, X. Lu, X. Zhang, Z. Xie, Y. Liu, B. J. Su, J. M. Chen, D. S. Su, W. Qi and S. Guo, *Chem*, 2020, **6**, 1443–1458.
14 M. J. Graham and M. Cohen, *J. Electrochem. Soc.*, 1972, **119**, 879.
15 X. Song, N. Li, H. Zhang, L. Wang, Y. Yan, H. Wang, L. Wang and Z. Bian, *ACS Appl. Mater. Interfaces*, 2020, **12**, 17519–17527.
16 C. Tang, L. Chen, H. Li, L. Li, Y. Jiao, Y. Zheng, H. Xu, K. Davey and S. Z. Qiao, *J. Am. Chem. Soc.*, 2021, **143**, 7819–7827.
17 P. Cao, X. Quan, X. Nie, K. Zhao, Y. Liu, S. Chen, H. Yu and J. G. Chen, *Nat. Commun.*, 2023, **14**, 1–12.
18 E. Jung, H. Shin, B. H. Lee, V. Efremov, S. Lee, H. S. Lee, J. Kim, W. Hooch Antink, S. Park, K. S. Lee, S. P. Cho, J. S. Yoo, Y. E. Sung and T. Hyeon, *Nat. Mater.*, 2020, **19**, 436–442.
19 Q. Zhang, X. Tan, N. M. Bedford, Z. Han, L. Thomsen, S. Smith, R. Amal and X. Lu, *Nat. Commun.*, 2020, **11**, 4181.
20 R. Li, S. Yang, Y. Zhang, G. Yu, C. Wang, C. Chen, G. Wu, R. Sun, G. Wang, X. Zheng, W. Yan, G. Wang, D. Rao and X. Hong, *Cell Rep. Phys. Sci.*, 2022, **3**, 100788.
21 A. M. Dimiev, K. Shukhina and A. Khannanov, *Carbon*, 2020, **166**, 1–14.
22 G. H. Major, N. Fairley, P. M. A. Sherwood, M. R. Linford, J. Terry, V. Fernandez and K. Artyushkova, *J. Vac. Sci. Technol., A*, 2020, **38**, 061203.
23 A. P. Grosvenor, M. C. Biesinger, R. S. C. Smart and N. S. McIntyre, *Surf. Sci.*, 2006, **600**, 1771–1779.
24 M. C. Biesinger, B. P. Payne, L. W. M. Lau, A. Gerson and R. S. C. Smart, *Surf. Interface Anal.*, 2009, **41**, 324–332.
25 M. C. Biesinger, B. P. Payne, A. P. Grosvenor, L. W. M. Lau, A. R. Gerson and R. S. C. Smart, *Appl. Surf. Sci.*, 2011, **257**, 2717–2730.
26 M. C. Biesinger, L. W. M. Lau, A. R. Gerson and R. S. C. Smart, *Phys. Chem. Chem. Phys.*, 2012, **14**, 2434–2442.
27 T. R. Gengenbach, G. H. Major, M. R. Linford and C. D. Easton, *J. Vac. Sci. Technol., A*, 2021, **39**, 013204.
28 A. Svalova, V. Brusko, E. Sultanova, M. Kirsanova, T. Khamidullin, I. Vakhitov and A. M. Dimiev, *Appl. Surf. Sci.*, 2021, **565**, 150503.
29 S. Galyaltdinov, A. Svalova, V. Brusko, M. Kirsanova and A. M. Dimiev, *Molecules*, 2022, **27**, 5637.

Open Access Article. Published on 28 March 2023. Downloaded on 12/5/2025 1:32:46 PM.
This article is licensed under a Creative Commons Attribution-NonCommercial 3.0 Unported Licence.

30 H. H. Huang, K. K. H. De Silva, G. R. A. Kumara and M. Yoshimura, *Sci. Rep.*, 2018, **8**, 2–10.
31 G. S. Bocharov, A. V. Eletskii and V. P. Mel, *Nanosyst.: Phys., Chem., Math.*, 2018, **9**, 98–101.
32 H. Tian, A. Wucher and N. Winograd, *J. Am. Soc. Mass Spectrom.*, 2016, **27**, 2014–2024.
33 S. Sui, X. Wang, X. Zhou, Y. Su, S. Riffat and C. jun Liu, *J. Mater. Chem. A*, 2017, **5**, 1808–1825.

 This journal is © The Royal Society of Chemistry 2023